AGU PUBLICATIONS

JGR

Journal of Geophysical Research: Space Physics

RESEARCH ARTICLE
10.1002/2016JA023226

Key Points:
- Ice shelf vibrations are studied as cause of persistent atmospheric wave activity in Antarctic MLT
- Simple physical models of long-period vibrations of floating ice shelves are developed
- The hypothesis of the Ross Ice Shelf-MLT coupling explains key features of recent lidar observations

Correspondence to:
O. A. Godin,
oagodin@nps.edu

Citation:
Godin, O. A., and N. A. Zabotin (2016), Resonance vibrations of the Ross Ice Shelf and observations of persistent atmospheric waves, *J. Geophys. Res. Space Physics*, *121*, 10,157–10,171, doi:10.1002/2016JA023226.

Received 23 JUL 2016
Accepted 17 SEP 2016
Accepted article online 20 SEP 2016
Published online 10 OCT 2016

Resonance vibrations of the Ross Ice Shelf and observations of persistent atmospheric waves

Oleg A. Godin[1] and Nikolay A. Zabotin[2]

[1]Department of Physics, Naval Postgraduate School, Monterey, California, USA, [2]Department of Electrical, Computer, and Energy Engineering, University of Colorado Boulder, Boulder, Colorado, USA

Abstract Recently reported lidar observations have revealed a persistent wave activity in the Antarctic middle and upper atmosphere that has no counterpart in observations at midlatitude and low-latitude locations. The unusual wave activity suggests a geographically specific source of atmospheric waves with periods of 3–10 h. Here we investigate theoretically the hypothesis that the unusual atmospheric wave activity in Antarctica is generated by the fundamental and low-order modes of vibrations of the Ross Ice Shelf (RIS). Simple models are developed to describe basic physical properties of resonant vibrations of large ice shelves and their coupling to the atmosphere. Dispersion relation of the long surface waves, which propagate in the floating ice sheet and are responsible for its low-order resonances, is found to be similar to the dispersion relation of infragravity waves in the ice-free ocean. The phase speed of the surface waves and the resonant frequencies determine the periods and wave vectors of atmospheric waves that are generated by the RIS resonant oscillations. The altitude-dependent vertical wavelengths and the periods of the acoustic-gravity waves in the atmosphere are shown to be sensitive to the physical parameters of the RIS, which can be difficult to measure by other means. Predicted properties of the atmospheric waves prove to be in a remarkable agreement with the key features of the observed persistent wave activity.

1. Introduction

Recently, observations were reported of rather unusual atmospheric wave activity in Antarctica [*Chen et al.*, 2016]. With a lidar instrument operating at McMurdo, Antarctica, *Chen et al.* [2016] observed persistent, large-amplitude acoustic-gravity waves with 3–10 h periods and vertical wavelengths between 20 and 30 km from the stratosphere to lower thermosphere. Remarkably, these waves were present during every lidar observation throughout the 5 year observation period at McMurdo, and no similar atmospheric wave activity was ever observed at midlatitude and low-latitude locations [*Chen et al.*, 2016].

From tropospheric to mesospheric heights, dominant nontidal atmospheric waves are believed to be generated by moist convection, shear flow instabilities, jets, atmospheric fronts, and interaction of winds with the Earth's topography [*Gossard and Hooke*, 1975; *Fritts and Alexander*, 2003; *Geller et al.*, 2013; *Vincent et al.*, 2013; *Plougonven and Zhang*, 2014; *Alexander et al.*, 2016]. At high latitudes, auroral activity also makes a significant contribution [*Hunsucker*, 1982; *Oyama and Watkins*, 2012]. These wave sources are intermittent and are not known to generate persistent wave activity or a narrow range of vertical wavelengths.

In this paper, we propose a possible explanation for the cause of the observed persistent atmospheric wave activity at McMurdo, Antarctica. The observations were made in the immediate vicinity of the Ross Ice Shelf (RIS) (Figure 1). The RIS occupies the southern part of the Ross Sea and is the world's largest ice shelf. Presence of ice sheets introduces additional vibration modes [*Press and Ewing*, 1951; *Holdsworth and Glynn*, 1978, 1981; *Sergienko*, 2013; *MacAyeal et al.*, 2015], which can potentially enhance conversion of oceanic wave energy into atmospheric waves. Exceptionally large horizontal dimensions of the RIS facilitate radiation by the ice shelf oscillations of long atmospheric waves that can reach thermospheric altitudes. Previous studies revealed waves in the middle and upper atmosphere that were generated by various wave processes in the ocean and solid earth such as tsunamis [*Artru et al.*, 2005; *Makela et al.*, 2011; *Galvan et al.*, 2012; *Komjathy et al.*, 2012; *Occhipinti et al.*, 2013], earthquakes [*Lognonné*, 2010; *Maruyama et al.*, 2012; *Astafyeva et al.*, 2013; *Occhipinti et al.*, 2013; *Garcia et al.*, 2014; *Jin et al.*, 2014], volcanic eruptions [*Tahira*, 1995; *Watada and Kanamori*, 2010], and background infragravity waves in the ocean [*Godin et al.*, 2015; *Zabotin et al.*, 2016].

We hypothesize that the persistent atmospheric waves in mesosphere and lower thermosphere are related to the ice cover and, specifically, to low-frequency vibration resonances of the RIS. By analyzing several idealized

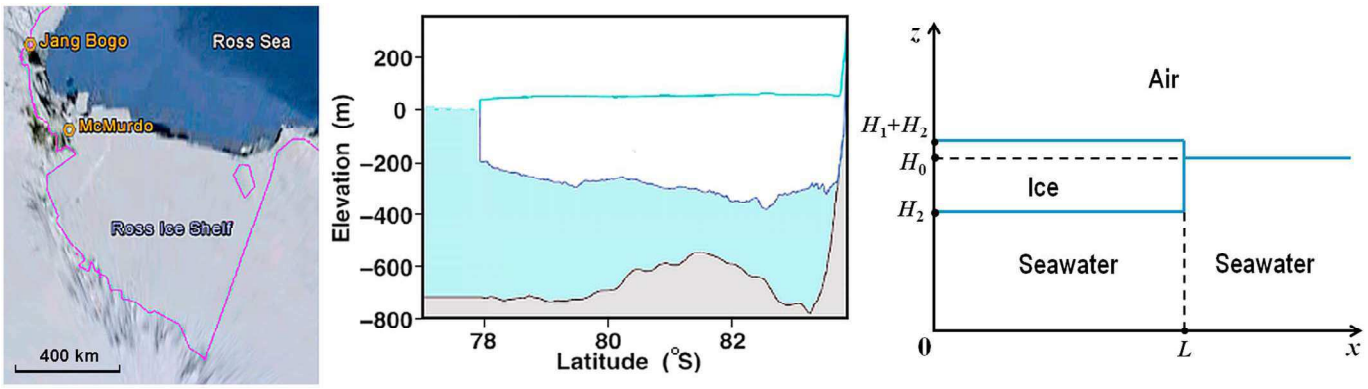

Figure 1. Ross Ice Shelf. (left) Google Earth image of the Ross Ice Shelf area. The yellow hexahedrons are locations of two Antarctic stations, McMurdo and Jang Bogo. An approximate grounding line of the shelf is shown by the magenta line. (middle) A transect of the shelf's ice/water/bedrock geometry along a line roughly orthogonal to the Ross Ice Shelf front (adapted from *Bromirski et al.* [2015]). Horizontal axis is compressed by a factor of about 700 compared to the vertical one. (right) Simplified geometry of the ice shelf that is used for analytical modeling of wave processes. The ice shelf grounding line and the ice front are perpendicular to the plane of the figure. L is the distance between the grounding line and the ice front. H_1 and H_2 are the thicknesses of the ice and the water-filled cavity beneath the ice; H_0 is the depth of ice-free water.

models of the coupled ice shelf-ocean system, we show that the temporal and spatial scales of atmospheric waves, which are radiated by the lowest-order modes of RIS vibrations, are consistent with the lidar observations of *Chen et al.* [2016] at McMurdo, Antarctica, that "the raw temperature data from the stratosphere to the lower thermosphere (about 30–115 km) exhibit persistent, dominant, large-amplitude waves with nontidal periods of ~3–10 h and vertical wavelengths of ~20–30 km."

Vibrations of floating glaciers are primarily studied in connection with iceberg calving and ice shelf stability [*Holdsworth and Glynn*, 1978, 1981; *MacAyeal et al.*, 2006; *Sergienko*, 2013; *Papathanasiou et al.*, 2015]. In that context, resonances with periods of less than about 30 s, which can be efficiently excited by sea swell and lead to the glacier breakup, are of primarily interest. In contrast, the fundamental mode and other low-order (hence longer period) resonances are most relevant to problem of origin of the persistent atmospheric wave activity, which has periods of several hours. To make an analytical treatment of the problem possible, we simplify geometry of the ice shelf. We will model RIS as a homogeneous rectangular plate of constant thickness, which is grounded on one (southern) side, faces the ocean on another (northern) side, and is supported by solid earth on the other (east and west) sides. Seafloor will be modeled as a rigid horizontal plane. We will be interested in long waves with horizontal wavelengths that are much larger than the ocean depth and the ice thickness.

Below, a Cartesian coordinate system is used with horizontal coordinates x and y and a vertical coordinate z. The vertical coordinate z is zero on the seafloor and increases upward. The ice shelf grounding line (the south edge of the ice shelf) is located at $x=0$. The ice front (the north edge of the ice shelf) is located at $x=L$. The east and west edges of the ice shelf are at $y=\pm L_y/2$, $0<x<L$.

The paper is organized as follows. In section 2, low-frequency oscillations of the RIS are studied in a traditional thin-plate, long-wave approximation. To overcome some physically undesirable limitations of this approach, a layered-fluid approximation is introduced and investigated in section 3. A simple model of generation of waves in the atmosphere by oscillations of large ice shelves is applied in section 4 to evaluate kinematic parameters of the forced atmospheric waves. Effects of Earth's rotation on the RIS resonant vibrations and resulting atmospheric waves are studied in section 5. Section 6 summarizes our findings.

2. Ice Shelf Vibrations in the Thin-Plate Approximation

Vibrations of ice shelves and ice tongues are usually described mathematically in the thin-beam (assuming that the wavefield depends on a single Cartesian horizontal coordinate) or thin-plate (where the wavefield can be a generic function of horizontal coordinates) approximations [*Press and Ewing*, 1951; *Wadhams*, 1973; *Holdsworth and Glynn*, 1978, 1981; *Williams and Robinson*, 1981; *Squire et al.*, 1995; *Squire*, 2007; *Sergienko*, 2013; *Papathanasiou et al.*, 2015]. In these approximations, vertical motions are averaged, and the problem

dimensionality is decreased. Vertical displacement $w(x, y, t)$ of a thin plate and velocity potential $\phi(x, y, t)$ of fluid motion in the cavity below the plate satisfy simultaneous partial differential equations [*Holdsworth and Glynn*, 1978, 1981; *Squire et al.*, 1995; *Sergienko*, 2013; *Papathanasiou et al.*, 2015]:

$$\rho_1 H_1 \frac{\partial^2 w}{\partial t^2} = \nabla_h^2 \left(D \nabla_h^2 w\right) - \rho_2 g w - \rho_2 \frac{\partial \phi}{\partial t}, \tag{1}$$

$$\frac{\partial w}{\partial t} = -\nabla_h \cdot (H_2 \nabla_h \phi), \quad \nabla_h = \left(\frac{\partial}{\partial x}, \ \frac{\partial}{\partial y}, \ 0\right). \tag{2}$$

Here t is time, ρ_1 and ρ_2 are densities of ice and water, H_1 is ice thickness, and H_2 is the thickness of the water-filled cavity beneath the ice (Figure 1). The flexural rigidity D of the plate is given by

$$D = E H_1^3 / 12\left(1 - \nu^2\right), \tag{3}$$

where E is the dynamic modulus of elasticity of the ice in bending, and ν is Poisson's ratio. Compressibility of water and ice is not taken into account [*Holdsworth and Glynn*, 1978, 1981; *Squire et al.*, 1995; *Sergienko*, 2013; *Papathanasiou et al.*, 2015]. This is justified as long as the phase speed of wave solutions to equations (1) and (2) is small compared to the velocity of compressional waves in water (~1500 m/s) and ice (~3500 m/s).

In the case of a uniform plate of constant thickness ($H_1 = \text{const.}$, $\rho_1 = \text{const.}$, and $D = \text{const.}$) and constant depth of a homogeneous fluid ($H_2 = \text{const.}$ and $\rho_2 = \text{const.}$), equations (1) and (2) have plane-wave solutions with dependence $\exp(ik_x x + ik_y y - i\omega t)$ on horizontal coordinates and time. For the plane waves, differential equations (1), (2) reduce to the algebraic equation [*Squire et al.*, 1995; *Sergienko*, 2013]:

$$D k^6 + \left(\rho_2 g - \rho_1 \omega^2 H_1\right) k^2 = \rho_2 \omega^2 / H_2. \tag{4}$$

Equation (4) relates wave number $k = (k_x{}^2 + k_y{}^2)^{1/2}$ and circular frequency ω of the plane waves and has the meaning of the dispersion relation of free waves in the coupled ice-ocean system, when there are no nonhorizontal boundaries. When viewed in 3-D, the plane waves are horizontally propagating surface waves.

Equation (4) is cubic with respect to k^2, and its analytic solutions are readily available and are given, e.g., by Cardano's formula [*Korn and Korn*, 1968]. We are interested in the fundamental mode and low-order modes of the RIS vibrations. In these modes, $k \sim L^{-1}$ and is very small. Below, we obtain long-wave asymptotics, equation (5), of the free-wave dispersion relation directly from equation (4). The same result can be also obtained —but with much more algebra—from Cardano's formula in the limit $\omega \to 0$.

For waves with a bounded phase speed $c \equiv \omega/k$, frequency $\omega \to 0$ when $k \to 0$. In the long-wave limit, it is sufficient to retain only the lowest-order term, $\rho_2 g k^2$, in the left side of equation (4). Then, we obtain rather simple dispersion relation:

$$\omega = k\sqrt{g H_2}. \tag{5}$$

This is the only solution to equation (4) that gives a finite, nonzero phase speed in the limit $k \to 0$. It follows from equations (4) and (5) that neglecting the term $\rho_1 H_1 \omega^2$ compared to $\rho_2 g$ and $D k^6$ compared to $\rho_2 g k^2$ in equation (4) is justified as long as $L \gg H_1 + H_2$ and the shear wave speed in the plate (i.e., in ice) is small compared to $(g L^4 H_1{}^{-3})^{1/2}$. These conditions are easily met for the RIS and other large ice shelves.

The dispersion relation equation (5) for long free waves in the coupled ice shelf-ocean system coincides with the dispersion relation of long waves in ice-free water of depth H_2. Hence, flexural-gravity waves propagate within ice horizontally with the speed of infragravity waves [*Webb et al.*, 1991; *Godin et al.*, 2014; *Ardhuin et al.*, 2014] in an ice-free ocean. In this approximation, neither flexural rigidity nor inertia of the ice shelf has any effect on the wave propagation speed. The free waves are not dispersive; their phase and group speeds have frequency independent value $(g H_2)^{1/2}$ according to equation (5).

In an unbounded floating ice shelf, the wave frequency and wave number vary continuously in equation (5). In the case of a finite ice shelf, appropriate boundary conditions need to be imposed at the ice grounding line, on the ice front, and at the side boundaries. The boundary conditions select discrete values of wave vector $\mathbf{k}$ and, through equation (5), determine resonant frequencies of the ice shelf. We assume that the ocean is limited by rigid vertical walls at the grounding line and the side boundaries. Then

$$\partial\phi/\partial x = 0, \quad x = 0 \tag{6}$$

and

$$\partial\phi/\partial y = 0, \quad y = \pm L_y/2. \tag{7}$$

Ocean depth H_0 in ice-free ocean beyond the ice front is related to H_1 and H_2 by the condition of hydrostatic equilibrium, which gives $H_0 = H_2 + H_1\,\rho_1/\rho_2$. Let fluid motion in the ice-free ocean be described by the velocity potential $\phi_0(x, y, t)$. At the ice front we impose the following boundary conditions:

$$\varphi = \varphi_0, \quad x = L \tag{8}$$

and

$$H_2\frac{\partial\varphi}{\partial x} = H_0\frac{\partial\varphi_0}{\partial x}, \quad x = L. \tag{9}$$

Although highly idealized, the boundary conditions (6)–(9) are the conditions that are normally employed when considering linear dynamics of ice shelves in the long-wave approximation [*Squire et al.*, 1995; *Sergienko*, 2010; *Papathanasiou et al.*, 2015]. Equation (8) expresses continuity of pressure in fluid at $x = L$. Equation (9) expresses continuity of mass flux through the plane $x = L$ and ensures conservation of the mass of fluid in the long-wave approximation.

Potentials that satisfy the boundary conditions (6) and (7) and the radiation condition at $x \to \infty$ are

$$\varphi(x,y) = A_1\cos\left(\frac{2\pi l y}{L_y}\right)\cos k_{1x}x, \quad k_{1x} = \sqrt{\frac{\omega^2}{gH_2} - \frac{4\pi^2 l^2}{L_y^2}}, \quad 0 < x < L, \tag{10}$$

$$\varphi_0(x,y) = A_0\cos\left(\frac{2\pi l y}{L_y}\right)e^{ik_{0x}(x-L)}, \quad k_{0x} = \sqrt{\frac{\omega^2}{gH_0} - \frac{4\pi^2 l^2}{L_y^2}}, \quad x > L, \tag{11}$$

where A_1 and A_0 are arbitrary constants, $\mathrm{Im}k_{0x} \geq 0$, and $l = 0, 1, 2, \ldots$. Time dependence $\exp(-i\omega t)$ is assumed and suppressed. Equation (11) describes an infragravity wave [*Webb et al.*, 1991; *Godin et al.*, 2014; *Ardhuin et al.*, 2014] that is propagating in ice-free ocean away from the ice shelf.

Substitution of equations (10) and (11) into boundary conditions (8) and (9) on the ice front gives two simultaneous linear algebraic equations for unknown A_1 and A_0. Nontrivial solutions of the simultaneous algebraic equations exist when

$$\tan k_{1x}L = -ik_{0x}H_0/k_{1x}H_2. \tag{12}$$

Equation (12) is the dispersion relation of low-order ice shelf resonances in the thin-plate approximation. It is expected that the resonance oscillations of the RIS are excited by tides [*Padman et al.*, 2003; *Bromirski et al.*, 2015], incident ocean waves [*Holdsworth and Glynn*, 1978, 1981; *MacAyeal et al.*, 2006; *Sergienko*, 2010; *Bromirski et al.*, 2010; *Bromirski and Stephen*, 2012; *Bromirski et al.*, 2015; *Papathanasiou et al.*, 2015], and possibly by wind. Specific mechanisms of the excitation and amplitudes of the RIS oscillations are beyond the scope of this paper.

Consider the resonances that do not involve horizontal motion along the ice front; $l = 0$ for these resonances. Then, the right side of equation (12) is independent of frequency and solutions are readily obtained analytically:

$$\omega_n = L^{-1}\sqrt{gH_2}\left[\pi\left(n + \frac{1}{2}\right) + i\zeta\right], \quad \zeta = \frac{1}{2}\ln\frac{H_1\rho_1/H_2\rho_2}{\left(1 + \sqrt{1 + H_1\rho_1/H_2\rho_2}\right)^2}, \quad n = 0, 1, 2, \ldots \tag{13}$$

Note that $\zeta < 0$. Only complex solutions ω_n exist at $l = 0$. Complexity of the resonance frequency ω_n means that after being excited by an external action, resonant oscillations decay in time: $|\exp(-i\omega_n t)| = \exp(\zeta t)$. Spatially, the amplitude of the resonance oscillations increases with distance from the grounding line according to equation (10).

For some $l \neq 0$, L, and L_y, dispersion equation (12) may admit real-valued solutions for resonance frequencies provided that $2\pi l(gH_2)^{1/2}\omega^{-1} < L_y < 2\pi l(gH_0)^{1/2}\omega^{-1}$.

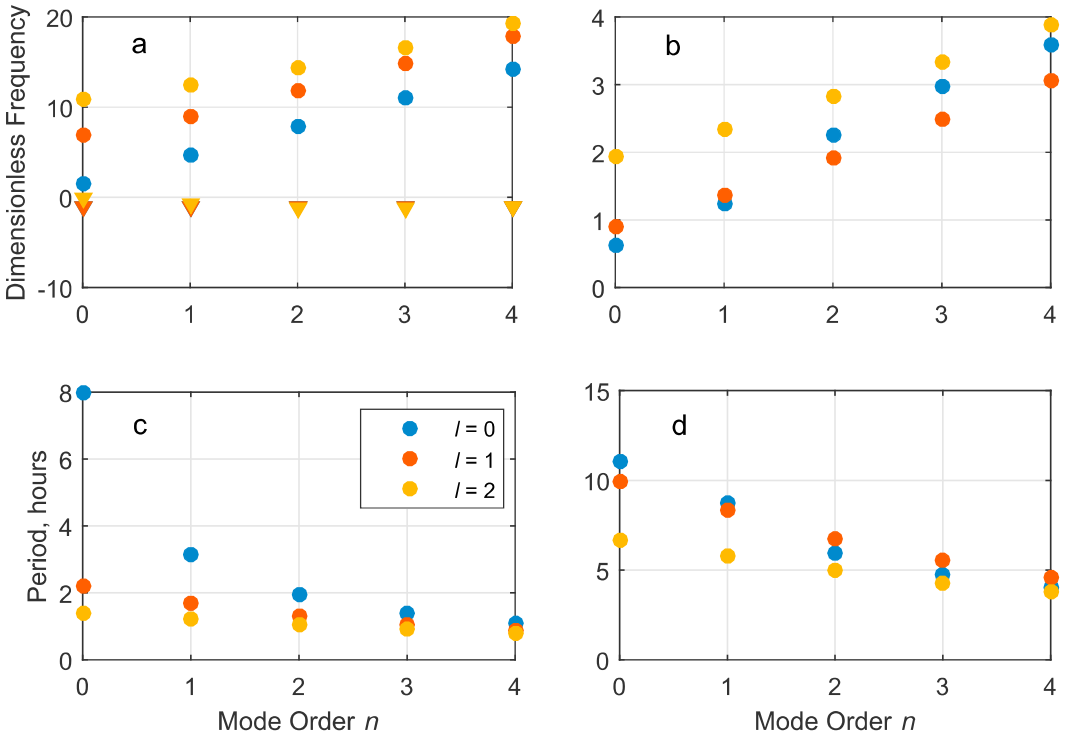

Figure 2. Fundamental and other low-order resonant vibrations of the Ross Ice Shelf. (a) Dimensionless resonant frequencies $\omega_{n,l}L(gH_2)^{-1/2}$ of the RIS oscillations that are calculated for different mode orders n, $l = 0, 1, 2, \ldots$ in the thin-plate approximation as roots of the dispersion relation equation (12). Real and imaginary parts of the dimensionless frequencies are shown by circles and triangles, respectively. (b) Same as in Figure 2a but using the layered fluid approximation instead of the thin-plate approximation. Resonant frequencies are calculated as roots of the dispersion relation equation (28) and are real valued. (c) Periods of the resonance oscillations that are calculated in the thin-plate approximation and adjusted for the Earth's rotation according to equation (41). (d) Same as in Figure 2c but using the layered fluid approximation instead of the thin-plate approximation. The RIS parameters assumed in calculations are $L = 550$ km, $L_y = 800$ km, $H_1 = 300$ m, $H_2 = 400$ m, and $\rho_2/\rho_1 = 0.9$; the value of the Coriolis parameter f_C is taken for the latitude of 77°. Color in all panels marks the transversal mode order l as shown in Figure 2c legend.

The fundamental mode of ice shelf vibrations corresponds to $l = 0$ and $n = 0$. From equations (5) and (13) for the fundamental mode we find

$$\omega_0 = \frac{\sqrt{gH_2}}{L}\left(\frac{\pi}{2} + i\zeta\right), \quad \mathbf{k} = \frac{1}{L}\left(\frac{\pi}{2} + i\zeta, 0, 0\right), \quad T_0 = \frac{2\pi}{\mathrm{Re}\omega_0} = \frac{4L}{\sqrt{gH_2}}. \tag{14}$$

As expected, k is of the order of L^{-1}. T_0 has the meaning of the period of resonance oscillations. Periods $T_n = 2\pi/\mathrm{Re}\ \omega_n$ are progressively shorter for higher-order resonances according to equation (13). Using $L = 550$ km and $H_2 = 400$ m to estimate the longest period of the RIS resonant vibrations, from equation (14) we obtain $T_0 \approx 9.8$ h, which is close to the reported longest period (10–10.6 h) of persistent atmospheric waves observed at McMurdo, Antarctica [*Chen et al.*, 2016]. The periods of the RIS resonance vibrations will be further discussed in section 5, where the effects of Earth's rotation are taken into account.

Figure 2a illustrates solutions of equation (12) for different values of l. For each n, the real part of the resonance frequency $\omega_{n,l}$ increases with l. Note a large difference between periods of the fundamental and the other modes of resonant oscillations. At $l = 0$, $\mathrm{Re}\ \omega_1 = 3\ \mathrm{Re}\ \omega_0$; the real parts of all frequencies $\omega_{n,l}$ are even larger than $\mathrm{Re}\ \omega_1$ when $l > 0$. Imaginary parts of the resonance frequencies $\omega_{n,l}$ only weakly depend on n and l when $l > 0$. However, $\mathrm{Im}\ \omega_{0,2} = 0$, and this mode of resonant oscillations does not decay in time.

3. Ice Shelf Vibrations in the Layered Fluid Approximation

While it is expected that flexural rigidity of ice has little effect on long waves [*Squire et al.*, 1995; *Papathanasiou et al.*, 2015], the absence in equation (5) of any inertial effect of the ice motion on free wave propagation is

surprising and cannot be justified physically. To overcome this drawback of the thin-plate approximation, one has to account for the vertical structure of the wave motion in the coupled ice shelf-ocean system and, specifically, rapid variations with z of the horizontal component of the wave-induced particle velocity in the vicinity of the ice-water interface. Here this is done approximately by neglecting shear rigidity of ice and modeling the latter as an incompressible fluid with density ρ_1 that is smaller than water density ρ_2.

Consider waves with harmonic dependence $\exp(ik_x x + ik_y y - i\omega t)$ on horizontal coordinates and time. Vertical dependencies of pressure p and vertical displacement w in fluid satisfy equations:

$$\frac{\partial p}{\partial z} = \rho\omega^2 w, \quad \frac{\partial w}{\partial z} = \frac{k^2 p}{\rho\omega^2}; \tag{15}$$

and the boundary conditions $w = 0$ on the seafloor $z = 0$ and $p = \rho_1 g w$ on the free surface $z = H_1 + H_2$ [see, e.g., *Godin*, 2012]. Solving equation (15) with the boundary condition on the rigid seafloor, one finds

$$w = A\sinh kz, \quad p = \rho_2\omega^2 k^{-1}\cosh kz, \quad 0 < z < H_2, \tag{16}$$

$$w = B_1 e^{kz} + B_2 e^{-kz}, \quad p = \rho_1\omega^2 k^{-1}\left(B_1 e^{kz} - B_2 e^{-kz}\right), \quad H_2 < z < H_1 + H_2, \tag{17}$$

where A and $B_{1,2}$ are arbitrary constants. By imposing the boundary condition on the free surface and the conditions of continuity of w and $p - \rho g w$ on the fluid-fluid interface $z = H_2$ [*Godin*, 2012], one obtains from equations (16) and (17) the dispersion equation of surface gravity waves in a horizontally unbounded layered fluid:

$$\frac{\rho_2}{\rho_1}\left(\coth kH_2 - \frac{kg}{\omega^2}\right)\left(1 - \frac{\omega^2}{kg}\coth kH_1\right) = \frac{\omega^2}{kg} - \frac{kg}{\omega^2}. \tag{18}$$

For long waves such that $k(H_1 + H_2) \ll 1$, the dispersion relation equation (18) simplifies and gives a quadratic equation

$$c^4 - g(H_1 + H_2)c^2 + g^2 H_1 H_2(1 - \rho_1/\rho_2) = 0 \tag{19}$$

for c^2, where $c = \omega/k$. In this limit,

$$B_1 = -B_2 = A\rho_2/2\rho_1. \tag{20}$$

Solutions of equation (19) define the phase speeds of "fast" (with the plus sign) and "slow" (with the minus sign) long gravity waves:

$$c = \sqrt{\frac{g}{2}(H_1 + H_2)\left[1 \pm \sqrt{1 - \frac{4H_1 H_2}{(H_1 + H_2)^2}\left(1 - \frac{\rho_1}{\rho_2}\right)}\right]}. \tag{21}$$

For the fast wave, the ratio $c/\sqrt{g(H_1 + H_2)}$ varies between $\sqrt{\left(1 + \sqrt{\rho_1/\rho_2}\right)/2}$, when $H_1 H_2 \to 0$ and 1, when $H_1 = H_2$. The range of the variations is rather narrow when $1 - \rho_1/\rho_2 \ll 1$. For the slow wave, the ratio $c/\sqrt{g(H_1 + H_2)}$ varies between 0, when $H_1 H_2 \to 0$, and $\sqrt{\left(1 - \sqrt{\rho_1/\rho_2}\right)/2}$, when $H_1 = H_2$.

On the ice front, which is now modeled as a boundary of two-layer fluid and a single layer of fluid 2 (water), we impose the following boundary conditions (compare with equations (8) and (9)):

$$\int_{H_2}^{H_1+H_2} v_x(x = L - 0, y, z)\mathrm{d}z = 0, \tag{22}$$

$$\int_0^{H_2} v_x(x = L - 0, y, z)\mathrm{d}z = \int_0^{H_0} v_x(x = L + 0, y, z)\mathrm{d}z, \tag{23}$$

and

$$\int_0^{H_1+H_2} p(x = L - 0, y, z)\mathrm{d}z = \int_0^{H_0} p(x = L + 0, y, z)\mathrm{d}z. \tag{24}$$

Here v_x is the x component of the wave-induced particle velocity. Equations (22) and (23) insure mass conservation for fluids 1 and 2, respectively. Equation (24) expresses the balance of forces applied to the boundary $x = L$.

Taking into account the rigid wall conditions at $\{x = 0, 0 < z < H_1 + H_2\}$ and using equations (16), (17), and (20), at $0 < x < L$ we find

$$v_x = \omega(A_1 \sin k_{1x}x + A_2 \sin k_{2x}x)\cos\left(\frac{2\pi l y}{L_y}\right), \quad k_{jx} = \sqrt{\frac{\omega^2}{c_j^2} - \frac{4\pi^2 l^2}{L_y^2}}, \quad 0 < z < H_2, \tag{25}$$

$$v_x = \omega\frac{\rho_2}{\rho_1}(A_1 \sin k_{1x}x + A_2 \sin k_{2x}x)\cos\left(\frac{2\pi l y}{L_y}\right), \quad H_2 < z < H_1 + H_2, \tag{26}$$

$$p = -i\omega^2\rho_2\left(\frac{A_1}{k_{1x}}\cos k_{1x}x + \frac{A_2}{k_{2x}}\cos k_{2x}x\right)\cos\left(\frac{2\pi l y}{L_y}\right), \quad 0 < z < H_1 + H_2, \tag{27}$$

Here $j = 1, 2$; $c_1 > c_2$ are phase speeds of the fast and slow gravity waves as given by equation (21); and $A_{1,2}$ are unknown constants, which describe amplitudes of the fast and slow gravity waves; $l = 0, 1, 2, \ldots$ characterizes the zonal structure of resonant oscillations and has the same meaning as in section 2.

Only one surface gravity wave is present at $x > L$. It is described by equation (11). Note that $v_x = \partial\phi_0/\partial x$ and $p = i\omega\rho_2\phi_0$ at $x > L$.

Substitution of equations (11) and (25)–(27) into boundary conditions equations (22)–(24) gives a set of three linear algebraic equations for unknown amplitudes A_1, A_2, and A_0. Nontrivial solutions of the algebraic equations exist when

$$k_{1x}\tan k_{1x}L = k_{2x}\tan k_{2x}L. \tag{28}$$

Equation (28) is the dispersion relation of ice shelf resonances in the fluid model. As expected, equation (28) indicates that in addition to ice shelf dimensions, both the ice thickness and water depth as well as the ice-water density ratio affect the frequencies of ice shelf resonances. This is in contrast to the thin-plate model that we considered in section 2.

Equation (28) gives real-valued resonance frequencies when k_{1x} and k_{2x} are either simultaneously real or simultaneously imaginary. In particular, one obtains real resonance frequencies ω_n, $n = 0, 1, 2, \ldots$, when $l = 0$. It follows from equation (21) that ${c_2}^2/{c_1}^2 \ll 1$ in the ice shelf problem because the ice and water density difference is relatively small. Then, for the fundamental mode we find from equation (28)

$$\omega_0 \approx \frac{\pi c_2}{L}\left(1 + \frac{c_2^2}{c_1^2}\right). \tag{29}$$

Terms of the third order in the ratio c_2/c_1 are neglected in equation (29) compared to unity. Each mode of resonance vibrations contains fast and slow surface waves. The relative weights of the slow and fast waves are determined by the ratio of constants A_2 and A_1 in equations (25)–(27). It follows from equations (22), (26), and (29) that $A_2 \gg A_1$ in the fundamental mode, i.e., slow waves with $k = \omega/c_2$ dominate in ice shelf vibrations in this resonance.

To estimate the longest period of resonance oscillations of the RIS, we take $L = 550$ km, $H_1 = 300$ m, and $H_2 = 400$ m (see Figure 1) and obtain $T_0 = 2\pi/\omega_0 \approx 22.7$ h. However, the atmospheric waves that are generated by slow surface waves in the ice shelf are unlikely to propagate to high altitudes due to dissipation in air and the critical level filtering, which are briefly discussed in section 4. Another solution of equation (28) gives a resonance, which is expected to generate atmospheric waves much more efficiently because the fast waves are dominant in that case. When $c_2/c_1 \ll 1$ and $l = 0$, equation (28) has solutions in the vicinity of points, where $k_{1x}L = \pi(n + 1/2)$. The lowest-order resonance in this series has the frequency

$$\omega \approx \frac{\pi c_1}{2L}\left(1 + \frac{c_2}{c_1}\cot\left(\frac{\pi c_1}{2c_2}\right)\right). \tag{30}$$

For the set of parameters that we have chosen to represent the RIS, equation (30) gives wave period $T \approx 6.3$ h. This solution corresponds to $n = 2$, $l = 0$ in Figures 2b and 2d, which show numerical solutions of equation (28).

An improved description of the ice shelf interaction with ocean in the underice cavity in the layered fluid model leads to a richer set of long-period resonant oscillations than in the thin-plate model. For representative parameters of the RIS, equation (28) gives nondecaying resonances at $l = 0, 1, 2$. Comparison of Figures 2a

and 2b shows that the difference in periods between the fundamental mode ($n = l = 0$) and other low-order modes of resonant oscillations is much smaller in the layered fluid model than in the thin-plate model. Note that $\omega_{n,1}$ and $\omega_{n,2}$ increase with n slower than $\omega_{n,0}$ (Figure 2b). At $n > 1$, vibration modes with a zonal structure ($l > 0$) can have longer periods than respective modes without dependence of the ice displacement on the coordinate y along the ice front.

We postpone comparison of the resonance periods that are predicted in the layered fluid model and the periods of persistent atmospheric waves observed at McMurdo, Antarctica [*Chen et al.*, 2016], until section 5, where effects of Earth's rotation are taken into account.

4. Properties of Atmospheric Waves

Waves that propagate along the surface of the ocean or ice shelf generate perturbations in the atmosphere. These perturbations are propagating or evanescent atmospheric waves depending on the frequency and phase speed of waves on the surface. Because air density is small compared to the water and ice densities, to first order one can neglect the effect of atmospheric loading on long waves in the ocean. Then, one can investigate the nature of induced atmospheric perturbations by using the properties of waves on the surface that were predicted without taking the atmospheric loading into account [*Godin et al.*, 2015].

Acoustic-gravity waves (AGWs) in the atmosphere have the dispersion relation [*Godin*, 2014, 2015]

$$m^2 = \frac{\omega_d^2}{c_s^2} - \frac{\gamma^2 g^2}{4c_s^4} - k^2\left[1 - \frac{(\gamma-1)g^2}{\omega_d^2 c_s^2}\right], \tag{31}$$

where c_s and $\mathbf{u}$ are the sound speed and wind velocity, $\gamma \approx 1.4$ is the ratio of specific heats in air at constant pressure and constant volume, (k_x, k_y, m) and ω are the AGW wave vector and frequency, $\mathbf{k} = (k_x, k_y, 0)$ is the horizontal wave vector, and $\omega_d = \omega - \mathbf{k}\cdot\mathbf{u}$ is the intrinsic frequency. Here we disregard the effect of dissipative processes on the AGW dispersion relation. When atmosphere is horizontally stratified and stationary, i.e., γ, c_s, and $\mathbf{u}$ are independent of horizontal coordinates and time, ω and $\mathbf{k}$ remain constant, while m varies with height. Strictly speaking, AGWs reduce to gravity waves and acoustic waves in the limits where fluid compressibility or buoyancy becomes negligible [*Gossard and Hooke*, 1975]. Often, AGWs with frequencies $|\omega_d| < (\gamma-1)^{1/2} g/c_s$ and $|\omega_d| > \gamma g/2c_s$ are loosely referred to as gravity waves and infrasound, respectively. (With this loose terminology—which we will not use—the atmospheric waves that are discussed further in this section would be called gravity waves.)

Atmospheric perturbations that are generated by surface waves have the same frequency ω and horizontal wave vector $\mathbf{k}$ as the surface waves. The sign of m^2 in equation (31) determines whether AGWs are propagating ($m^2 > 0$) or evanescent ($m^2 < 0$). Consider first AGWs in the absence of wind. From equation (31) we find

$$m^2 = \frac{(\gamma-1)g^2}{c^2 c_s^2}\left[1 - \frac{\gamma^2 c^2}{4(\gamma-1)c_s^2}\right] - k^2\left(1 - \frac{c^2}{c_s^2}\right), \tag{32}$$

where $c = \omega/k$. For the fundamental and low-order ice shelf resonances considered in sections 2 and 3, c is frequency independent and is small compared to the sound speed c_s in air. Then, the quantity in brackets in the right side of equation (32) is close to 1. The term with k^2 in the right side of equation (32) is small compared to the term $(\gamma-1)g^2/c^2 c_s{}^2$ for all waves with frequencies $\omega \ll g/c_s$, i.e., for waves with periods longer than about 10 min. This condition is easily met by the fundamental and low-order ice shelf resonances considered in sections 2 and 3. Hence, these resonance vibrations of ice shelves generate upward propagating atmospheric waves. Their vertical wavelength

$$\lambda_z = \frac{2\pi}{m} \approx \frac{2\pi c_s c}{g}\left(\gamma - 1 - \frac{\gamma^2 c^2}{4c_s^2}\right)^{-1/2} \tag{33}$$

is moderately sensitive to height and varies approximately proportional to the square root of absolute temperature of air. This is consistent with the observation by *Chen et al.* [2016] that changes in λ_z are typically within the factor of 1.5 from the stratosphere to lower thermosphere. As discussed above, typical values of c in different models are between $(gH_2)^{1/2}$ and $(gH_1 + gH_2)^{1/2}$ (except for slow surface waves in the layered fluid model), or about 50–90 m/s for the RIS. According to equation (33), it translates into λ_z values of about 20–30 km. This is in very good agreement with the observed values [*Chen et al.*, 2016].

According to equation (31), one needs to replace c with $|c - u_k|$ in equations (32) and (33) in order to take the wind into account. Here u_k is the projection of the wind velocity **u** on the direction of vector **k**. The effect of wind on the atmospheric waves generated by ice-shelf vibrations is threefold. First, AGWs are strongly dissipated in the vicinity of the critical height where $\omega_d = 0$ or, equivalently, $c = u_k$. Therefore, winds filter out slower waves, which encounter critical heights between the ice surface and the observation altitude. Second, variations of wind velocity with altitude contribute, in addition to temperature variations, to changes in the vertical wavelength of AGWs with height and in time. Third, winds can complicate the anisotropy of the field of atmospheric waves. In the absence of winds, the longest-period atmospheric waves, which are generated by the fundamental mode of ice shelf vibrations, are expected to propagate meridionally. Winds change the group speed and propagation direction of AGWs with a given **k** and, through the critical level filtering [*Gossard and Hooke*, 1975; *Fritts and Alexander*, 2003] and changes in dissipation rate [*Godin*, 2014], affect the azimuthal distribution of AGW power flux. Despite these potentially significant effects, winds do not change the period of atmospheric waves that are generated by ice shelf vibrations. The range of vertical wavelengths λ_z is little changed by winds as long as the ranges of variation of c and $|c - u_k|$ are similar. For predominantly zonal winds, this is expected to be the case for the fundamental mode of the RIS vibrations and lower-order modes with $k_y = 0$.

We supplement these theoretical considerations with calculations for a realistic model of the Antarctic atmosphere at the time of observations (Figure 3). Wind velocity profiles at McMurdo were generated by the Horizontal Wind Model 2014 (HWM14) model [*Drob et al.*, 2015] for 1 day in June 2014. The wind velocity experiences strong and rapid variations, especially at altitudes above 35 km. To obtain a background wind profile that is suitable to model propagation of waves with periods of 3–10 h, the output of the HWM14 model was averaged over 1 day and smoothed by calculating a running average over 15 km range of altitudes (Figure 3a). The zonal component of the background wind (not shown) was found to be an order of magnitude stronger than the meridional component at altitudes from the sea level to 110 km. The NRLMSISE-00.2 model [*Picone et al.*, 2002] was utilized to obtain an average profile of temperature for the same day (Figure 3b). The dispersion equation (31) of atmospheric waves was used to calculate the vertical wavelength $\lambda_z = 2\pi/m$ (Figures 3c and 3d). The calculations demonstrated that strong zonal winds block upward propagation of atmospheric waves that were generated by the RIS resonances with $l \neq 0$. The resonances with $l = 0$ generate atmospheric waves with $k_y = 0$; these waves are not sensitive to zonal winds. Figures 3c–3e refer to waves with $k_y = 0$.

Figure 3c illustrates the altitude dependence of λ_z when the thin-plate approximation is employed to find the RIS resonant vibrations. Meridional component of the wind velocity makes the wavelengths different for waves with opposite signs of the x component, k_x, of the wave vector. Within the 30–115 km altitude range of the *Chen et al.* [2016] observations, the predicted wavelengths for both k_x signs are within the range of 17–26 km. This is close to the observed range of 20–30 km [*Chen et al.*, 2016]. In agreement with theoretical considerations, λ_z proves to be insensitive to the mode order n of the RIS resonant vibrations.

In the layered fluid approximation, fast and slow waves in ice contribute to generation of atmospheric waves. Atmospheric waves that are generated by slow waves in ice are much shorter than the atmospheric waves generated by the fast waves (Figure 3d) and, as has been already mentioned, are expected to be strongly attenuated by dissipative processes in the atmosphere [*Gossard and Hooke*, 1975; *Fritts and Alexander*, 2003; *Godin*, 2014]. Fast waves generate atmospheric waves with $23\ \text{km} < \lambda_z < 33\ \text{km}$ (Figure 3d), which is consistent with observations of *Chen et al.* [2016]. Approximate equation (33) provides a good estimate for the λ_z range (Figure 3d).

The results presented in Figures 3c and 3d are insensitive to n and, hence, to wave period. However, as discussed in the next section, the latter conclusion is valid only for waves with periods less than about 5 h.

5. Effects of Earth Rotation

So far, we have ignored possible effects of Earth rotation on atmospheric waves and oscillations in the coupled ocean-ice shelf system. This can be justified only for waves with periods much smaller than the period $T_e = 24$ h of the Earth rotation. In practice, the rotation effects are usually negligible for waves with periods less than a few hours. This condition is certainly not met by the longer-period part of the persistent

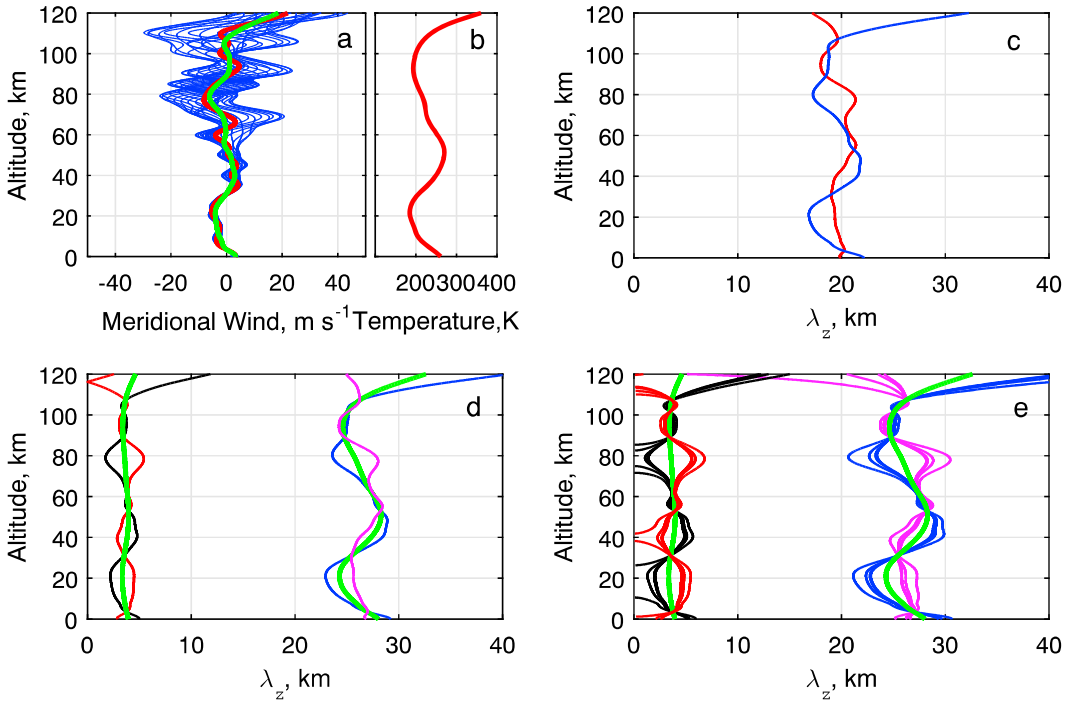

Figure 3. Vertical wavelength of the atmospheric waves that are generated by resonant vibrations of the Ross Ice Shelf. (a) Altitude profiles of the meridional wind at McMurdo, Antarctica, as provided by the HWM14 model [*Drob et al.*, 2015] for 1 day in June 2014. Blue lines are the wind profiles obtained with 1 h time increments; red line is the profile averaged over one day; green line shows the time-averaged wind profile smoothed over 15 km altitude intervals. The latter profile has been used in our calculations. (b) Average temperature profile as provided by the NRLMSISE-00.2 model [*Picone et al.*, 2002] for the same day. (c) Altitude dependence of the vertical wavelength λ_z of the atmospheric wave calculated for the RIS resonances with $l = 0$ and $n = 0$, 1 that are predicted in the thin-plate approximation. Earth's rotation is not taken into account. Red and blue curves correspond to opposite directions of the horizontal wave vector. Curves for different n overlap and cannot be distinguished on the scale of the plot. (d) Same as in Figure 3c but for the RIS resonances that are predicted in the layered fluid approximation. The two groups of curves correspond to the slow and fast waves as defined by equation (21). The colors (red and black for the slow wave, magenta and blue for the fast wave) distinguish solutions with the opposite directions of the horizontal wave vector. The green curves correspond to the approximate analytical solution equation (33) in the absence of wind. Curves that are calculated for different n overlap and are indistinguishable in the plot. (e) Same as in Figure 3d but with the Earth's rotation taken into account. Notation is the same as in the Figure 3d, but now $n = 0$, 1, 2, 3 and the curves corresponding to different n do not overlap.

atmospheric wave activity observed at McMurdo [*Chen et al.*, 2016]. In this section, we evaluate the effects of Earth rotation in the *f* plane approximation [*Gill*, 1982], where fluid motion in a noninertial reference frame is described by including in the Euler equation the Coriolis force due to vertical component of the angular velocity of the Earth's rotation.

In the *f* plane approximation, linearized equations of wave motion in a moving, compressible fluid in a gravity field [*Godin*, 1997], become

$$\nabla p + \rho\frac{\mathrm{d}^2\mathbf{w}}{\mathrm{d}t^2} + (\mathbf{w}\cdot\nabla)\nabla p_0 - (p + \mathbf{w}\cdot\nabla p_0)\frac{\nabla p_0}{\rho c_s^2} + 2\rho\Omega\times\left[\frac{\mathrm{d}\mathbf{w}}{\mathrm{d}t} - (\mathbf{w}\cdot\nabla)\mathbf{u}\right] = 0, \tag{34}$$

$$\nabla\cdot\mathbf{w} + (p + \mathbf{w}\cdot\nabla p_0)/\rho c_s^2 = 0. \tag{35}$$

Here $\times$ denotes cross product of vectors, $\mathrm{d}/\mathrm{d}t = \partial/\partial t + \mathbf{u}\cdot\nabla$ is the convective time derivative, $\mathbf{u}$ is the velocity of background flow, p_0, ρ, and c_s are the pressure, density, and sound speed in the absence of waves, and $\mathbf{w}$ is oscillatory displacement of fluid parcels. In terms of the oscillatory displacement, wave-induced perturbations in fluid velocity are $\mathbf{v} = \mathrm{d}\mathbf{w}/\mathrm{d}t - (\mathbf{w}\cdot\nabla)\mathbf{u}$. In equation (34) $\mathbf{\Omega} = (0,\ 0,\ f_C/2)$ is the angular velocity, $f_C = 4\pi T_e^{-1}\sin\theta$ is the Coriolis parameter, and θ is latitude. The Coriolis parameter equals twice the vertical component of the angular velocity of the Earth's rotation. Equations (34) and (35) apply to ideal fluids with an arbitrary equation of state [*Godin*, 1997].

Consider waves with harmonic dependence $\exp(ik_x x + ik_y y - i\omega t)$ on horizontal coordinates and time in a horizontally stratified fluid with a horizontal background flow. Then p_0, ρ, $\mathbf{u}$, and c_s are functions of the vertical coordinate z only, $dp_0/dz = -\rho g$, and equations (34) and (35) simplify to become

$$\frac{\partial p}{\partial z} + \frac{gp}{c_s^2} = w_z\left(\rho\omega_d^2 + g\frac{d\rho}{dz} + \frac{g^2}{c_s^2}\right), \tag{36}$$

$$\nabla_h p = \rho\omega_d^2 \mathbf{w}_h + 2\rho\boldsymbol{\Omega}\times(i\omega_d \mathbf{w} + w_z d\mathbf{u}/dz), \tag{37}$$

$$i\mathbf{k}\cdot\mathbf{w} + \frac{\partial w_z}{\partial z} + \frac{p - \rho g w_z}{\rho c_s^2} = 0. \tag{38}$$

Here $\nabla_h = (\partial/\partial x,\ \partial/\partial y,\ 0)$, $\mathbf{w}_h = (w_x,\ w_y,\ 0)$, and $\mathbf{k} = (k_x,\ k_y,\ 0)$ is the horizontal wave vector. By eliminating unknown $\mathbf{w}_h$ from simultaneous equations (37) and (38), one obtains

$$\frac{\partial w_z}{\partial z} - \frac{g w_z}{c_s^2} - \frac{2w_z}{\omega_d^2 - 4\Omega^2}\left[\frac{2\Omega^2}{\omega_d}\frac{d\omega_d}{dz} + i\mathbf{k}\cdot\left(\boldsymbol{\Omega}\times\frac{d\mathbf{u}}{dz}\right)\right] = \left(\frac{k^2}{\omega_d^2 - 4\Omega^2} - \frac{1}{c_s^2}\right)\frac{p}{\rho}. \tag{39}$$

When supplemented by appropriate boundary conditions, first-order differential equations (36) and (39) allow one to determine unknown vertical dependencies of the wave-induced pressure perturbation p and vertical displacement w_z. After these are found, all other characteristics of the wavefield can be calculated in terms of p and w_z. When $\Omega = 0$, equations (36) and (39) reduce to known governing equations for AGW in nonrotating fluids, see equations (5) and (6) in *Godin* [2012]. (Specifically, equation (36) coincides with equation (5) in *Godin* [2012], and equation (39) with $\Omega = 0$ gives equation (6) in *Godin* [2012]). In the particular case of incompressible, quiescent fluid of constant density, equations (36) and (39) reduce to equation (15) that we used in section 3. (In section 3 the notation w was used for the vertical displacement w_z.)

Note that when written in terms of p and w_z, boundary conditions on horizontal fluid-fluid interfaces as well as on rigid and pressure-release surfaces contain neither $\mathbf{k}$ nor ω [*Godin*, 1997, 2012]. Let us consider motionless layered fluids with piecewise continuous variations of ρ and c_s and a uniform background flow. When $d\mathbf{u}/dz = 0$, governing equations for waves in rotating and nonrotating fluids differ only by k being replaced with

$$k^{(r)} = k\left(1 - f_C^2/\omega_d^2\right)^{-1/2} \tag{40}$$

in equation (39). Hence, dispersion equations of surface waves and other normal modes in horizontally unbounded rotating fluids differ from respective dispersion equations in nonrotating fluids by replacing k with $k^{(r)}$. In particular, equation (21) remains valid for long waves in a two-layered incompressible rotating fluid but with $c = \omega/k^{(r)}$ rather than $c = \omega/k$. This is consistent with known results [*Gill*, 1982] for single-layered incompressible rotating fluids. Equation (40) shows that surface waves, which are nondispersive in the absence of rotation, become dispersive, when $f_C \neq 0$, and are strongly dispersive, when $\omega_d \sim f_C$.

More generally, in the long-wave limit (i.e., at $k \to 0$) the dispersion equation of surface waves with finite, nonzero phase speed c has the form $k = \omega/c$ in nonrotating fluids. Let the surface wave give a resonance with frequency ω_n and wave vector $\mathbf{k}_n$ in the nonrotating, quiescent ($\mathbf{u} = 0$) layered fluid with vertical boundaries.

Equation (40) suggests that in the presence of rotation, the resonance frequency $\omega_n^{(r)} = ck^{(r)} = ck_n\left(1 - f_C^2/\omega_n^{(r)2}\right)^{-1/2} = \omega_n\left(1 - f_C^2/\omega_n^{(r)2}\right)^{-1/2}$. Hence,

$$\omega_n^{(r)} = \sqrt{\omega_n^2 + f_C^2}. \tag{41}$$

Equation (41) is a simple relation between the resonance frequencies ω_n, which are calculated in a nonrotating fluid, and the frequencies $\omega_n^{(r)}$, which are observed on rotating Earth.

To be more specific, consider the fluid model of the ice shelf that was introduced in section 3. For simplicity, here we limit our analysis to waves without dependence on the horizontal coordinate y, which is parallel to the ice front. We assume that such waves satisfy boundary conditions on the side boundaries $y = \pm L_y/2$ of the ice shelf. Repeating the derivations that are outlined in section 3, at $0 < x < L$ we obtain from equations (36) and (39)

$$v_x = \omega(A_1 \sin k_1 x + A_2 \sin k_2 x), \quad k_j = \sqrt{\omega^2 - f_C^2}/c_j, \quad 0 < z < H_2, \tag{42}$$

$$v_x = \omega \frac{\rho_2}{\rho_1}(A_1 \sin k_1 x + A_2 \sin k_2 x), \quad H_2 < z < H_1 + H_2, \tag{43}$$

$$p = -i(\omega^2 - f_C^2)\rho_2 \left(\frac{A_1}{k_1}\cos k_1 x + \frac{A_2}{k_2}\cos k_2 x\right), \quad 0 < z < H_1 + H_2 \tag{44}$$

instead of equations (25)–(27). Equations (42)–(44) describe long-wave motion of an ice shelf in the presence of rotation. At $x > L$, i.e., in the ocean without ice cover, equation (11) can no longer be used because wave motion is not potential in rotating fluids. Instead, from equations (36) and (39) we find

$$v_x = -i\omega A_0 \exp(ik_0 x), \quad k_0 = \sqrt{\omega^2 - f_C^2/gH_0}, \quad 0 < z < H_0, \tag{45}$$

$$p = -i(\omega^2 - f_C^2)\rho_2 A_0 \exp(ik_0 x), \quad 0 < z < H_0. \tag{46}$$

Boundary conditions on the ice front, equations (22)–(24), give a set of three linear algebraic equations for unknown constants A_0, A_1, and A_2 in equations (42)–(46). The dispersion relation of ice shelf resonances

$$k_1 \tan k_1 L = k_2 \tan k_2 L \tag{47}$$

is obtained as the condition of existence of nontrivial solutions of the algebraic equations.

Equation (47) is similar to the dispersion relation equation (28) in the no-rotation case except k_1 and k_2 in the presence of rotation are given by equation (42) instead of equation (25) with $l = 0$. A comparison of equations (25) and (42) verifies the relation equation (41) between the resonance frequencies of ice shelf vibrations in problems with and without rotation.

Now consider the influence of rotation on atmospheric waves. The terms with the angular velocity $\mathbf{\Omega}$ in the left side of equation (39) vanish in the limit $d\mathbf{u}/dz \to 0$ and are small in the case of slow, gradual variation of the wind velocity with altitude. The terms with $d\mathbf{u}/dz$ are inversely proportional to the spatial scale of the altitude dependence of wind velocity. This spatial scale serves as a large parameter in the asymptotic expansions that lead to the ray and Wentzel-Kramers-Brillouin (WKB) approximations [*Godin*, 2014, 2015]. Therefore, the terms with $d\mathbf{u}/dz$ have no effect on the AGW dispersion relation but will affect the Berry phase and wave amplitude in the ray and WKB approximations [see *Godin*, 2014, 2015]. Hence, AGW dispersion equation in rotating atmosphere is obtained from equation (31) by replacing k with $k^{(r)}$, equation (40):

$$m^2 = \frac{\omega_d^2}{c_s^2} - \frac{\gamma^2 g^2}{4c_s^4} - \frac{\omega_d^2 k^2}{\omega_d^2 - f_c^2}\left[1 - \frac{(\gamma - 1)g^2}{\omega_d^2 c_s^2}\right]. \tag{48}$$

This result agrees with a known dispersion equation [*Gossard and Hooke*, 1975, p. 112] for the particular case of waves in an isothermal, quiescent, rotating atmosphere.

We use the AGW dispersion equation (48) to address properties of atmospheric waves that are generated by resonance vibrations of ice shelves. Let $\mathbf{u} = 0$, $\omega > f_C$, and denote $c = k^{-1}(\omega^2 - f_C^2)^{1/2}$. In the case of ice shelf vibrations, c has the meaning of the phase speed of a long surface wave as calculated without account for rotation; c is frequency independent in the long-wave limit and small compared to the sound speed c_s in air. From equation (48) we find

$$m^2 = \frac{(\gamma - 1)g^2}{c^2 c_s^2}\left[1 - \frac{\gamma^2 c^2}{4(\gamma - 1)c_s^2}\right] - \frac{\omega^2}{c^2}\left(1 - \frac{c^2}{c_s^2}\right). \tag{49}$$

Equation (49) is quite similar to equation (32) that has been discussed in section 4 except in the right side of equation (49) we have $\omega^2 c^{-2} = k^2 + f_C^2 c^{-2}$ instead of k^2 in equation (32). As before, the term with ω^2 in the right side of equation (49) is small compared to the term $(\gamma - 1)g^2/c^2 c_s^2$ for all waves with frequencies $\omega \ll g/c_s$, or with periods longer than about 10 min. For the vertical wavelength of atmospheric waves we again obtain equation (33). Hence, Earth's rotation does not change any conclusions that are made in section 4 regarding the vertical structure of atmospheric waves as long as the wind speed is sufficiently small.

In contrast to the vertical structure of atmospheric waves radiated by ice shelf resonance vibrations, Earth's rotation has a significant effect on the frequencies of the atmospheric waves. The frequencies are determined

by resonant frequencies of the ice shelf. Equation (41) shows that the rotation increases resonance frequencies, and the effect is the stronger the lower the resonant frequency. We have $\omega_n^{(r)} \geq \max(\omega_n, f_C)$, and $\omega_n^{(r)} \approx f_C$ when $\omega_n \ll f_C$. In polar regions $2\pi/f_C$ is close to 12 h. Then equation (41) maps the range $3\,\mathrm{h} < T_n < 24\,\mathrm{h}$ of the ice-shelf resonant periods $T_n = 2\pi/\omega_n$, which are calculated in the nonrotating case, into the range $2.9\,\mathrm{h} < T_n^{(r)} < 10.7\,\mathrm{h}$ of resonant periods $T_n^{(r)} = 2\pi/\omega_n^{(r)}$ to be observed in polar regions.

Figure 2 complements these general considerations with numerical results obtained for a specific RIS model in the thin-plate (Figure 2c) and layered-fluid (Figure 2d) approximations. In the thin-plate approximation, the RIS is predicted to have two modes of resonant vibrations ($n = 0$, 1 and $l = 0$) that radiate atmospheric waves with periods in the 3–10 h range (Figure 2c). In the layered-fluid approximation, at least 15 modes of resonant vibrations ($0 \leq n \leq 4$ and $0 \leq l \leq 2$) fill this range of periods (Figure 2d). This is consistent with the diversity of atmospheric wave periods observed by *Chen et al*. [2016]. In the absence of rotation, $T_0 \approx 22.7$ h for the fundamental mode, see section 3. Due to effects of Earth's rotation, the fundamental mode period in Figure 2d decreases and proves to be very close to the upper bound of periods of the persistent atmospheric wave activity observed at McMurdo [see *Chen et al*., 2016, Figure 6]. This coincidence suggests that the upper bound of the observed periods is primarily determined by the Coriolis parameter rather than details of the resonant oscillations. The vertical wavelength $\lambda_z = 2\pi/m$, on the other hand, is sensitive to the phase speed c of the waves, which are responsible for resonant vibrations of the ice shelf.

Figure 3e illustrates the altitude dependence of the vertical wavelength of atmospheric waves, which is calculated from the dispersion equation (48) for the realistic atmospheric model shown in Figures 3a and 3b. The atmospheric waves in Figure 3e are generated by the RIS resonant vibrations, which are modeled in the layered-fluid approximation (Figure 2d). As in the nonrotating case (Figure 3d), upward propagation of waves with $k_y \neq 0$ is blocked by strong zonal winds, and only resonances with $l = 0$ are represented in Figure 3e.

Calculations confirm that the effect of Earth's rotation on λ_z is negligible in the absence of winds. However, the combined effect of the rotation and winds proves to be rather strong. In contrast to the nonrotating case (Figure 3d), there is a significant difference in λ_z values in atmospheric waves due to ice-shelf resonances with distinct mode orders n (Figure 3e). Due to Earth's rotation, numerous altitudes appear where $\lambda_z = 0$ for the atmospheric waves that are radiated by slow waves in the ice (Figure 3e). These altitudes are the critical levels where the waves are fully dissipated [*Gossard and Hooke*, 1975, pp. 170–181]. Presence of the critical levels adds to the argument made in section 4 for why slow waves in ice are not expected to contribute appreciably to the observed persistent atmospheric wave activity, especially at thermospheric altitudes. For atmospheric waves that are radiated by fast waves in the ice, the combined effect of Earth's rotation and wind leads to more diversity in vertical wavelengths and somewhat stronger altitude dependence (compare Figures 3d and 3e). At altitudes below 115 km, predicted λ_z values fill the 20–30 km range in an excellent agreement with observations of *Chen et al*. [2016].

6. Conclusions

Radiation of atmospheric waves by fundamental and other low-order resonance vibrations of large ice shelves is qualitatively similar to previously considered radiation of atmospheric waves by infragravity waves in ice-free water [*Godin et al*., 2015; *Zabotin et al*., 2016]. Properties of the persistent atmospheric wave activity, which are observed in Antarctica in the vicinity of the Ross Ice Shelf [*Chen et al*., 2016], differ from the properties of AGWs, which are directly generated by infragravity waves in an open ocean, because of differences in the power spectra of background infragravity waves [*Godin et al*., 2013; *Ardhuin et al*., 2014] and ice shelf vibrations. The key features of the persistent atmospheric wave activity reported by [*Chen et al*., 2016], including frequency band, vertical wavelength range, and weak variation of the vertical wavelength with height, can be explained by simplified models of the Ross Ice Shelf proposed in this paper.

It is hoped that the present work will serve as a motivation for in-depth studies of coupling between vibrations of ice shelves and waves in the upper and middle atmosphere at high latitudes. Further research involving detailed numerical simulations is necessary to account for actual shape of the ice shelf and variations in its thickness and ocean depth, which were ignored in the simplified models. As long as the atmospheric waves are generated by the ice shelf vibrations, they reveal the low-order resonances, which can be difficult to observe by other means [*Williams and Robinson*, 1981; *Padman et al*., 2003; *Bromirski and Stephen*, 2012;

Bromirski et al., 2015] because of their long periods and small surface slopes. The atmospheric waves are sensitive to geometrical and physical parameters of the RIS and carry information about its properties. It would be important to investigate which physical parameters of the ice shelf and its dynamics can be retrieved from lidar and radar observations of atmospheric waves.

Acknowledgments
We are grateful to the Editor, Michael Liemohn, and two anonymous referees for comments and suggestions that helped us to improve presentation. All data for this paper are properly cited and referred to in the reference list. The research reported in this paper was supported by the Basic Research Challenge program of the Office of Naval Research, award N000141310348 and utilized the research computing facility at the University of Colorado Boulder, which is supported by the National Science Foundation, award CNS-0821794.

References

Alexander, S. P., K. Sato, S. Watanabe, Y. Kawatani, and D. J. Murphy (2016), Southern Hemisphere extratropical gravity wave sources and intermittency revealed by a middle-atmosphere general circulation model, *J. Atmos. Sci.*, *73*(3), 1335–1349, doi:10.1175/JAS-D-15-0149.1.

Ardhuin, F., A. Rawat, and J. Aucan (2014), A numerical model for free infragravity waves: Definition and validation at regional and global scales, *Ocean Modelling*, *77*, 20–32, doi:10.1016/j.ocemod.2014.02.006.

Artru, J., V. Ducic, H. Kanamori, P. Lognonné, and M. Murakami (2005), Ionospheric detection of gravity waves induced by tsunamis, *Geophys. J. Int.*, *160*(3), 840–848, doi:10.1111/j.1365-246X.2005.02552.x.

Astafyeva, E., L. Rolland, P. Lognonné, K. Khelfi, and T. Yahagi (2013), Parameters of seismic source as deduced from 1 Hz ionospheric GPS data: Case study of the 2011 Tohoku-oki event, *J. Geophys. Res. Space Physics*, *118*, 5942–5950, doi:10.1002/jgra.50556.

Bromirski, P. D., A. Diez, P. Gerstoft, R. A. Stephen, T. Bolmer, D. A. Wiens, R. C. Aster, and A. Nyblade (2015), Ross ice shelf vibrations, *Geophys. Res. Lett.*, *42*, 7589–7597, doi:10.1002/2015GL065284.

Bromirski, P. D., O. V. Sergienko, and D. R. MacAyeal (2010), Transoceanic infragravity waves impacting Antarctic ice shelves, *Geophys. Res. Lett.*, *37*, L02502, doi:10.1029/2009GL041488.

Bromirski, P. D., and R. A. Stephen (2012), Response of the Ross Ice Shelf, Antarctica, to ocean gravity-wave forcing, *Ann. Glaciol.*, *53*(60), 163–172, doi:10.3189/2012AoG60A058.

Chen, C., X. Chu, J. Zhao, B. R. Roberts, Z. Yu, W. Fong, X. Lu, and J. A. Smith (2016), Lidar observations of persistent gravity waves with periods of 3–10 h in the Antarctic middle and upper atmosphere at McMurdo (77.83°S, 166.67°E), *J. Geophys. Res. Space Physics*, *121*, 1483–1502, doi:10.1002/2015JA022127.

Drob, D. P., et al. (2015), An update to the horizontal wind model (HWM): The quiet time thermosphere, *Earth Space Sci.*, *2*(7), 301–319, doi:10.1002/2014EA000089.

Fritts, D. C., and M. J. Alexander (2003), Gravity wave dynamics and effects in the middle atmosphere, *Rev. Geophys.*, *41*(1), 1003, doi:10.1029/2001RG000106.

Galvan, D. A., A. Komjathy, M. P. Hickey, P. Stephens, J. Snively, Y. Tony Song, M. D. Butala, and A. J. Mannucci (2012), Ionospheric signatures of Tohoku-Oki tsunami of March 11, 2011: Model comparisons near the epicenter, *Radio Sci.*, *47*, RS4003, doi:10.1029/2012RS005023.

Garcia, R. F., E. Doornbos, S. Bruinsma, and H. Hebert (2014), Atmospheric gravity waves due to the Tohoku-Oki tsunami observed in the thermosphere by GOCE, *J. Geophys. Res. Atmospheres*, *119*, 4498–4506, doi:10.1002/2013JD021120.

Geller, M. A., et al. (2013), A comparison between gravity wave momentum fluxes in observations and climate models, *J. Clim.*, *26*, 6383–6405, doi:10.1175/JCLI-D-12-00545.1.

Gill, A. E. (1982), *Atmosphere–Ocean Dynamics*, Academic Press, New York.

Godin, O. A. (1997), Reciprocity and energy theorems for waves in a compressible inhomogeneous moving fluid, *Wave Motion*, *25*(2), 143–167, doi:10.1016/S0165-2125(96)00037-6.

Godin, O. A. (2012), Acoustic-gravity waves in atmospheric and oceanic waveguides, *J. Acoust. Soc. Am.*, *132*(2), 657–669, doi:10.1121/1.4731213.

Godin, O. A. (2014), Dissipation of acoustic-gravity waves: An asymptotic approach, *J. Acoust. Soc. Am.*, *136*(6), EL411–EL417, doi:10.1121/1.4902426.

Godin, O. A. (2015), Wentzel–Kramers–Brillouin approximation for atmospheric waves, *J. Fluid Mech.*, *777*, 260–290, doi:10.1017/jfm.2015.367.

Godin, O. A., N. A. Zabotin, A. F. Sheehan, Z. Yang, and J. A. Collins (2013), Power spectra of infragravity waves in a deep ocean, *Geophys. Res. Lett.*, *40*, 2159–2165, doi:10.1002/grl.50418.

Godin, O. A., N. A. Zabotin, A. F. Sheehan, and J. A. Collins (2014), Interferometry of infragravity waves off New Zealand, *J. Geophys. Res. Oceans*, *118*, 1103–1122, doi:10.1002/2013JC009395.

Godin, O. A., N. A. Zabotin, and T. W. Bullett (2015), Acoustic-gravity waves in the atmosphere generated by infragravity waves in the ocean, *Earth Planets Space*, *67*, Art. 47, doi:10.1186/s40623-015-0212-4.

Gossard, E. E., and W. H. Hooke (1975), *Waves in the Atmosphere*, 456 p., Elsevier, Amsterdam.

Holdsworth, G., and J. Glynn (1978), Iceberg calving from floating glaciers by a vibrating mechanism, *Nature*, *274*(5670), 464–466, doi:10.1038/274464a0.

Holdsworth, G., and J. E. Glynn (1981), A mechanism for the formation of large icebergs, *J. Geophys. Res.*, *86*(NC4), 3210–3222, doi:10.1029/JC086iC04p03210.

Hunsucker, R. D. (1982), Atmospheric gravity waves generated in the high-latitude ionosphere: A review, *Rev. Geophys.*, *20*(2), 293–315, doi:10.1029/RG020i002p00293.

Jin, S., R. Jin, and J. H. Li (2014), Pattern and evolution of seismo-ionospheric disturbances following the 2011 Tohoku earthquakes from GPS observations, *J. Geophys. Res. Space Physics*, *119*, 7914–7927, doi:10.1002/2014JA019825.

Komjathy, A., D. A. Galvan, P. Stephens, M. D. Butala, V. Akopian, B. Wilson, O. Verkhoglyadova, A. J. Mannucci, and M. Hickey (2012), Detecting ionospheric TEC perturbations caused by natural hazards using a global network of GPS receivers: The Tohoku case study, *Earth Planets Space*, *64*(12), 1287–1294, doi:10.5047/eps.2012.08.003.

Korn, G. A., and T. M. Korn (1968), *Mathematical Handbook for Scientists and Engineers: Definitions, Theorems, and Formulas for Reference and Review*, 2nd ed., McGraw-Hill, New York.

Lognonné, P. (2010), Seismic waves from atmospheric sources and atmospheric/ionospheric signatures of seismic waves, in *Infrasound Monitoring for Atmospheric Studies*, pp. 281–304, Springer, Netherlands.

MacAyeal, D. R., et al. (2006), Transoceanic wave propagation links iceberg calving margins of Antarctica with storms in tropics and Northern Hemisphere, *Geophys. Res. Lett.*, *33*, L17502, doi:10.1029/2006GL027235.

MacAyeal, D. R., Y. Wang, and E. A. Okal (2015), Ambient seismic, hydroacoustic, and flexural gravity wave noise on a tabular iceberg, *J. Geophys. Res. Earth Surf.*, *120*, 200–211, doi:10.1002/2014JF003250.

Makela, J. J., et al. (2011), Imaging and modeling the ionospheric airglow response over Hawaii to the tsunami generated by the Tohoku earthquake of 11 March 2011, *Geophys. Res. Lett.*, *38*, L13305, doi:10.1029/2011GL047860.

Maruyama, T., T. Tsugawa, H. Kato, M. Ishii, and M. Nishioka (2012), Rayleigh wave signature in ionograms induced by strong earthquakes, *J. Geophys. Res.*, *117*, A08306, doi:10.1029/2012JA017952.

Occhipinti, G., L. Rolland, P. Lognonné, and S. Watada (2013), From Sumatra 2004 to Tohoku-Oki 2011: The systematic GPS detection of the ionospheric signature induced by tsunamigenic earthquakes, *J. Geophys. Res. Space Physics*, *118*, 3626–3636, doi:10.1002/jgra.50322.

Oyama, S., and B. J. Watkins (2012), Generation of atmospheric gravity waves in the polar thermosphere in response to auroral activity, *Space Sci. Rev.*, *168*(1–4), 463–473, doi:10.1007/s11214-011-9847-z.

Padman, L., S. Erofeeva, and I. Joughin (2003), Tides of the Ross Sea and Ross Ice Shelf cavity, *Antarctic Sci.*, *15*(1), 31–40, doi:10.1017/S0954102003001032.

Papathanasiou, T. K., A. E. Karperaki, E. E. Theotokoglou, and K. A. Belibassakis (2015), Hydroelastic analysis of ice shelves under long wave excitation, *Nat. Hazards Earth Syst. Sci.*, *15*(8), 1851–1857, doi:10.5194/nhess-15-1851-2015.

Picone, J. M., A. E. Hedin, D. P. Drob, and A. C. Aikin (2002), NRLMSISE-00 empirical model of the atmosphere: statistical comparisons and scientific issues, *J. Geophys. Res.*, *107*, 1468, doi:10.1029/2002JA009430.

Plougonven, R., and F. Zhang (2014), Internal gravity waves from atmospheric jets and fronts, *Rev. Geophys.*, *52*, 33–76, doi:10.1002/2012RG000419.

Press, F., and M. Ewing (1951), Theory of air-coupled flexural waves, *J. Appl. Phys.*, *22*(7), 892–899, doi:10.1063/1.1700069.

Sergienko, O. V. (2010), Elastic response of floating glacier ice to impact of long-period ocean waves, *J. Geophys. Res.*, *115*, F04028, doi:10.1029/2010JF001721.

Sergienko, O. V. (2013), Normal modes of a coupled ice-shelf/sub-ice-shelf cavity system, *J. Glaciology*, *59*(213), 76–80, doi:10.3189/2013JoG12J096.

Squire, V. A., J. P. Dugan, P. Wadhams, P. J. Rottier, and A. K. Liu (1995), Of ocean waves and sea ice, *Annu. Rev. Fluid Mech.*, *27*(1), 115–168, doi:10.1146/annurev.fl.27.010195.000555.

Squire, V. A. (2007), Of ocean waves and sea-ice revisited, *Cold Reg. Sci. Technol.*, *49*(2), 110–133, doi:10.1016/j.coldregions.2007.04.007.

Tahira, M. (1995), Acoustic resonance of the atmosphere at 3.7 Hz, *J. Atmospheric Sci.*, *52*(15), 2670–2674, doi:10.1175/1520-0469(1995)052<2670:AROTAA>2.0.CO;2.

Vincent, R. A., M. J. Alexander, B. K. Dolman, A. D. MacKinnon, P. T. May, S. Kovalam, and I. M. Reid (2013), Gravity wave generation by convection and momentum deposition in the mesosphere-lower thermosphere, *J. Geophys. Res. Atmospheres*, *118*, 6233–6245, doi:10.1002/jgrd.50372.

Wadhams, P. (1973), Attenuation of swell by sea ice, *J. Geophys. Res.*, *78*(18), 3552–3563, doi:10.1029/JC078i018p03552.

Watada, S., and H. Kanamori (2010), Acoustic resonant oscillations between the atmosphere and the solid earth during the 1991 Mt. Pinatubo eruption, *J. Geophys. Res.*, *115*(B12), B12319, doi:10.1029/2010JB007747.

Webb, S. C., X. Zhang, and W. Crawford (1991), Infragravity waves in the deep ocean, *J. Geophys. Res.*, *96*(C2), 2723–2736, doi:10.1029/90JC02212.

Williams, R. T., and E. S. Robinson (1981), Flexural waves in the Ross Ice Shelf, *J. Geophys. Res.*, *86*(C7), 6643–6648, doi:10.1029/JC086iC07p06643.

Zabotin, N. A., O. A. Godin, and T. W. Bullett (2016), Oceans are a major source of waves in the thermosphere, *J. Geophys. Res. Space Physics*, *121*, 3452–3463, doi:10.1002/2016JA022357.